A&A, 710, L18 (2026)
https://doi.org/10.1051/0004-6361/202660461

Astronomy & Astrophysics

LETTER TO THE EDITOR

Seismic signature of a magnetic field in the γ Doradus star KIC 2309579

S. Ihallaine[1,⋆], J. Ballot[1], F. Lignières[1], L. Ferrié[1], S. Charpinet[1], M. Galoy[2], and G. Li (李刚)[3]

[1] IRAP, Université de Toulouse, CNRS, CNES, 14 avenue Edouard Belin, 31400 Toulouse, France
[2] Max-Planck-Institut für Sonnensystemforschung, 37077 Göttingen, Germany
[3] Centre for Astrophysics, University of Southern Queensland, Toowoomba, QLD 4350, Australia

Received 16 April 2026 / Accepted 21 May 2026

ABSTRACT

Context. Internal magnetic fields have recently been detected and measured in the radiative core of red giant stars using asteroseismology. As they are one of the progenitors of red giant stars and exhibit high radial order gravity modes, γ Doradus stars may also hold detectable magnetic fields in their radiative envelope.

Aims. We aim to detect, for the first time, an internal magnetic field in a rapidly rotating γ Doradus star through its influence on the propagation of Kelvin gravito-inertial modes.

Methods. We used the seismic variable $\delta K_{\rm a}$, defined as a combination of Kelvin modes frequencies, which is sensitive to the presence of a magnetic field. Following the detection, we modeled the star oscillation spectrum while considering a magnetic component following a Bayesian approach.

Results. We found a magnetic signature in the radiative envelope of KIC 2309579. If located just above the core, in the layers that were previously convective, the magnetic field would reach ~4 kG.

Key words. asteroseismology – stars: magnetic field – stars: oscillations – stars: individual: KIC 2309579

1. Introduction

Over the past few decades, asteroseismology has emerged as a powerful tool for probing the interior of stars, and it has revealed crucial measurements of near-core rotations, ages, and masses. These measurements have shown that stellar models overestimate core rotation (Mosser et al. 2012; Ouazzani et al. 2019), which indicates that some physical phenomenon occurring in stars are missing in our models. Magnetic fields may be a major actor in the angular momentum transport within stars. Nevertheless, for a long time, only surface magnetic fields could be detected and studied using spectropolarimetry, leaving the study of the inner part of the fields inaccessible. Fuller et al. (2015) showed that a strong enough inner magnetic field hinders the propagation of gravity (g) modes and could explain the suppression of mixed dipolar modes observed in some red giants stars. More recently, magnetic fields have been detected and measured in the radiative core of several red giants stars (Li et al. 2022, 2023; Deheuvels et al. 2023; Hatt et al. 2024; Villate et al. 2026) and in the radiative envelope of a slowly rotating δ Scuti-γ Doradus star (Takata et al. 2026) using a seismic approach. These measurements provide key constraints for answering the question of angular momentum transport. The γ Doradus (γ Dor) stars are pulsating main-sequence (MS) late A- to early F-type stars with masses from 1.3 to 2 $M_\odot$ (Kaye et al. 1999). Their internal structure is composed of a convective core, a radiative envelope, and a shallow convective envelope. Although they exhibit high radial order gravito-inertial (g–i) modes, which are most affected by magnetic fields, there is currently no seismic evidence of inner magnetic fields in the typical rapidly rotating γ Dor stars. Their rotation periods, which are on the order of a day (Li et al. 2020), make it impossible to consider rotation as a perturbation, as is done for red giants (Li et al. 2022). The traditional approximation of rotation (Lee & Saio 1997), hereafter referred to as "TAR", has been used instead to study g–i modes of rapidly rotating stars, as its validity has been tested for the modes observed in γ Dor stars (Ballot et al. 2012; Ouazzani et al. 2017, 2020). Prat et al. (2019, 2020) studied the effect of dipolar magnetic fields on TAR g–i modes considering the Lorentz force as a perturbation, while Dhouib et al. (2022) treated the Lorentz force in a nonperturbative way for an axisymmetric toroidal field. Recently, Lignières et al. (2024) proposed a generalization to an arbitrary magnetic field of the perturbative approach and derived analytical forms of frequency shifts for g–i and Rossby modes. They also introduced a new seismic variable, which is specifically sensitive to magnetic fields: the difference of Kelvin mode frequencies $\delta K_{\rm a}$.

In the following, we first present the method for identifying magnetic star candidates thanks to the seismic variable $\delta K_{\rm a}$ and carry out the spectral analysis of such a star, KIC 2309579, in Sect. 2. We then present the modeling of the star oscillation spectrum considering a magnetic component as well as the corresponding results in Sect. 3. In Sect. 4, we investigate the properties of the inner magnetic field of KIC 2309579. Finally, we present a discussion and a conclusion in Sect. 5.

2. Identifying magnetic candidates

Kelvin modes are g–i equatorial prograde modes present in rotating stars. They are usually labeled by their degree ℓ and their azimuthal order $m = -\ell$, as they become prograde sectoral modes at zero rotation. Lignières et al. (2024) have introduced a seismic variable, $\delta K_{\rm a}$, defined as a combination between the

⋆ Corresponding author: selyan.ihallaine@utoulouse.fr

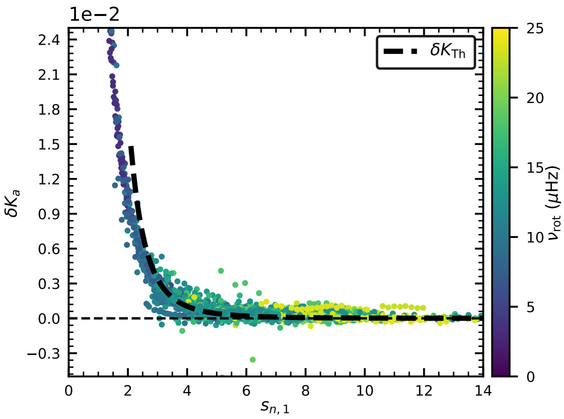

Fig. 1. Dimensionless seismic variable $\delta K_{\rm a}$ as a function of the spin parameter $s_{n,1}$ for the 155 γ Dor stars from the Li et al. (2020) catalog. A dashed black curve shows the asymptotic approximation $\delta K_{\rm Th}$ (see Lignières et al. 2024). Colors indicate the stellar rotation rate.

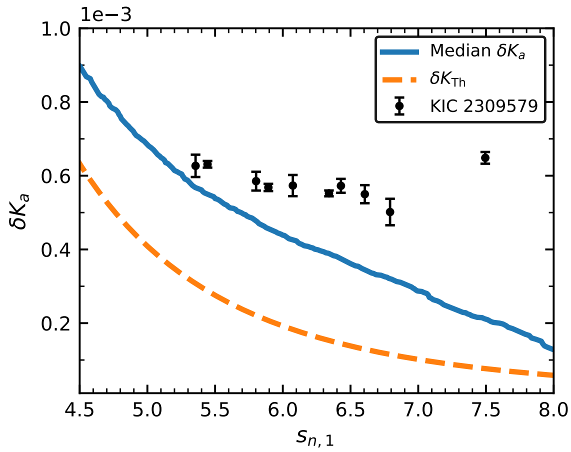

Fig. 2. Dimensionless seismic variable $\delta K_{\rm a}$ as a function of the spin parameter $s_{n,1}$ for modes identified in KIC 2309579. For comparison, we plot the median $\delta K_{\rm a}$ of the 155 stars (blue line) and the asymptotic approximation $\delta K_{\rm Th}$ (orange dashes).

frequencies of $\ell = 1$ and $\ell = 2$ Kelvin modes with the same radial order n, denoted $\nu_{n,\ell}$, normalized by twice the star rotation frequency $\nu_{\rm rot}$:

$$\delta K_{\rm a} = \frac{1}{2\nu_{\rm rot}}\left(\nu_{n,1} - \frac{1}{2}\,\nu_{n,2}\right). \tag{1}$$

In the absence of a magnetic field, asymptotic theory predicts that $\delta K_{\rm a}$ is the same function of the spin parameter $s_{n,1} = 2\nu_{\rm rot}/\nu^{\rm co}_{n,1}$, where $\nu^{\rm co}_{n,1}$ refers to the $\nu_{n,\ell}$ frequency in the corotation frame, for all γ Dor stars and that this function vanishes at high $s_{n,1}$. In contrast, the radial component of a magnetic field produces an increase of $\delta K_{\rm a}$ proportional to $s^3_{n,1}$. This property provides a simple method for detecting magnetic fields in γ Dor stars holding both $\ell = 1$ and $\ell = 2$ Kelvin modes.

2.1. Description of the analyzed γ Dor star sample

Li et al. (2020) analyzed 611 γ Dor stars observed by the *Kepler* space mission (Borucki et al. 2010). They found both $\ell = 1$ and $\ell = 2$ Kelvin modes among 155 of these stars. From a $\Delta P - P$ diagram fitting method, they determined the rotation frequencies and the buoyancy radii Π_0 of these stars. We identified the radial order of modes detected in these stars with the TAR and computed $\delta K_{\rm a}$ for this sample. Results are shown in Fig. 1. The data collapse around a single curve, independent of the rotation rate of the stars, that converges at high spin parameters toward the asymptotic relation calculated within the TAR and the Wentzel-Kramers-Brillouin (WKB) approximation, denoted $\delta K_{\rm Th}$. We thus searched for stars showing deviations from this general trend. Some points exhibit strong departures, but we have shown it is generally due to incorrect radial order identifications. We identified a few stars with a behavior compatible with what we expect from a magnetic field. In the rest of the paper, we present the detailed analysis of the best candidate, KIC 2309579.

2.2. Spectral analysis of KIC 2309579

In order to fully control all the steps of the analysis, we first reprocessed the *Kepler* light curve of KIC 2309579 downloaded from the MAST archive[1] in order to extract the oscillation frequencies using the `FELIX` code (Charpinet et al. 2010; Zong et al. 2016). We extracted the frequencies with a signal-to-noise ratio greater than 4.7, that is a 4σ detection level. The detailed result of the extraction is reported in Appendix D. As in Li et al. (2020), we identified $\ell = 1$ and $\ell = 2$ Kelvin modes in the ranges 13–17 μHz and 28–32 μHz. The mode identification was performed with the `GMorse` code (Christophe et al. 2018).

We excluded from the following analysis the frequencies that have high probabilities ($\leq 2\sigma$) to be linear combinations of two higher amplitude frequencies or harmonics of higher peaks. Figure 2 shows the $\delta K_{\rm a}$ of KIC 2309579 computed from this frequency list. For comparison, also plotted are the median $\delta K_{\rm a}$ of the 155 stars and $\delta K_{\rm Th}$. The values measured for KIC 2309579 exhibit a clear departure from the median of the whole sample and from $\delta K_{\rm Th}$. Furthermore, we found that this departure is compatible with a profile proportional to $s^3_{n,1}$, as expected for magnetic stars. The difference between $\delta K_{\rm Th}$ and the median $\delta K_{\rm a}$ can be partly explained by the limitations of the asymptotic theory (Lignières et al. 2024), but it could also result from a general magnetic behavior of the star sample. The small oscillatory behavior of the data is likely due to a glitch occurring near the convective core of the star. The variable $\delta K_{\rm a}$ is a good indicator of a candidate, but it has limitations: (i) Its results rely on an a priori determination of n, which can be biased by the presence of a magnetic field (Lignières et al. 2024). (ii) We only used 20 out of the 34 extracted frequencies (those that share a common n and have a different ℓ). In the following, we propose using a magnetic model to reproduce KIC 2309579 oscillation spectrum.

3. Spectrum model including magnetic field

Following an approach similar to the one used to analyze red giant stars by Villate et al. (2026), we fit all the observed mode frequencies with an asymptotic model that includes the effects of a magnetic field. We present the model in Sect. 3.1 and the results of the fit to the observations in Sect. 3.2.

3.1. Asymptotic model

In the absence of a magnetic field, we computed the frequencies of Kelvin modes within the TAR and used the WKB approximation in the radial direction. In this case, the non-perturbed

[1] https://archive.stsci.edu/missions-and-data/kepler

frequencies $\nu^0_{n,\ell}$ of modes are expressed through the equation

$$\frac{1}{\nu^0_{n,\ell} - m\nu_{\rm rot}} = \frac{\Pi_0}{\sqrt{\Lambda_\ell\left(s_{n,\ell}\right)}}\left(n + \epsilon_{g_\ell}\right), \tag{2}$$

where $\Lambda_\ell\,(s)$ are the Laplace tidal equation eigenvalues, Π_0 is the buoyancy radius of the star, and ϵ_{g_ℓ} is a phase offset for modes of degree ℓ (e.g., Berthomieu et al. 1978). Lignières et al. (2024) derived the perturbation of frequencies induced by a magnetic field not dominated by its azimuthal component for $\ell = 1$ and $\ell = 2$ Kelvin modes:

$$\nu_{n,1} = \nu^0_{n,1} + \nu_B \cdot s^3_{n,1}, \quad \nu_{n,2} = \nu^0_{n,2} + 4\nu_B \cdot s^3_{n,2}, \tag{3}$$

where $\nu_B = \dfrac{\mathcal{I} B^2_{\rm eq}}{(4\pi)^5 {\nu_{\rm rot}}^3}$ in the cgs system, with

$$\mathcal{I} = \int_{r_i}^{r_o} \frac{1}{\rho}\left(\frac{N}{r}\right)^3 {\rm d}r \Bigg/ \int_{r_i}^{r_o} \frac{N}{r}\,{\rm d}r \quad \text{and} \tag{4}$$

$$B^2_{\rm eq} = \int_{r_i}^{r_o} K_r(r)\,\langle B_r^2\rangle_\phi\,(\theta = \pi/2)\;{\rm d}r, \tag{5}$$

where ρ is the density, N the Brunt-Väisälä frequency, and r_i and r_o are respectively the inner and outer boundaries of the oscillation cavity. The factor $\mathcal{I}$ depends on the stellar structure along the oscillation cavity and $B^2_{\rm eq}$ is the radial and azimuthal average of the radial component of the magnetic field evaluated at the equator, where Kelvin modes are mainly concentrated for large spin parameters. The radial weight function, $K_r(r)$, is defined as

$$K_r(r) = \frac{1}{\rho}\left(\frac{N}{r}\right)^3 \Bigg/ \int_{r_i}^{r_o} \frac{1}{\rho}\left(\frac{N}{r}\right)^3 {\rm d}r. \tag{6}$$

Compared to Eqs. (30) and (31) in Lignières et al. (2024), we left out a $\propto 1/s$ term that appears to be negligible in front of the first-order terms. The model thus relies on five free parameters: Π_0, $\nu_{\rm rot}$, ϵ_{g_1}, ϵ_{g_2}, and ν_B.

3.2. Fitting the model to observations

We fit our model to the observed frequencies by following a Bayesian approach using the `ABIM` code (see Appendix A.2 for details). We obtained unimodal (almost normal) posterior distributions for all parameters. We compared the best-model frequencies, obtained from the median values of these distributions, to the observed ones. We plot the comparison in a so-called stretched period échelle diagram (Christophe et al. 2018) in Fig. 3. The best model is consistent with the observations. In a nonmagnetic TAR framework, the échelle diagrams represent mode periods sharing the same ℓ and m on a vertical line. In our case, the échelle diagrams, especially that of the $\ell = 1$ modes, show distinct curvatures due to the influence of the magnetic field on the higher periods. In the plot, we display the frequencies we excluded from the analysis, because they could be interpreted as frequency combinations. Some of them could nevertheless be modes since they are very close to modeled frequencies.

We then derived the posterior distribution of $\mathcal{I} B^2_{\rm eq}$ from those of ν_B and $\nu_{\rm rot}$. We thus measured that $\mathcal{I} B^2_{\rm eq} = 2.23 \pm 0.16 \times 10^{-20}\,{\rm cm\,s^{-2}\,g^{-1}\,G^2}$. In order to infer a magnetic field strength, we needed a stellar structure model of KIC 2309579.

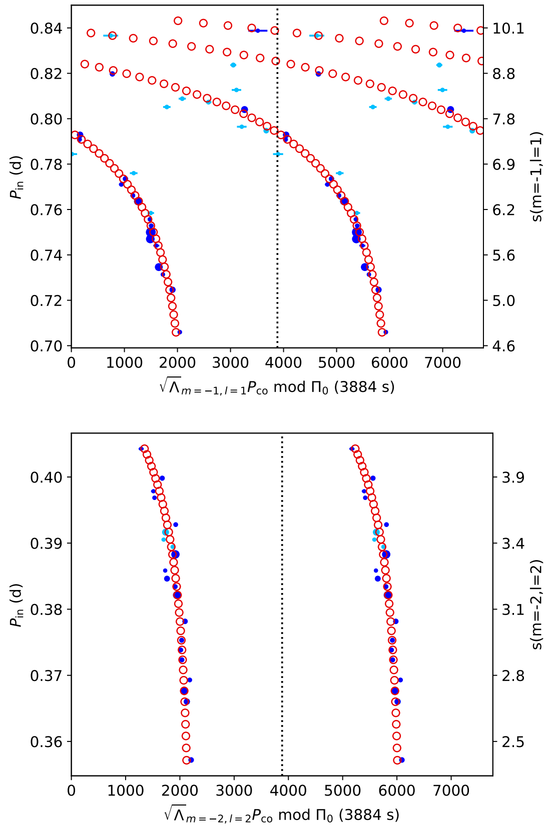

Fig. 3. Stretched period échelle diagram of $\ell = 1$ (top) and $\ell = 2$ (bottom) Kelvin mode frequencies. Navy blue dots indicate observed frequencies used for the analysis. Light blue dots represent observed frequencies that are possible frequency combinations and discarded for the analysis. Red circles are frequencies of the best model including a magnetic field. The size of the dots is proportional to the mode amplitude.

4. Magnetic field strength

We computed γ Dor star models with `CESAM2k20` (Morel 1997; Manchon et al. 2025) calibrated on the buoyancy radius of KIC 2309579 that we measured as well as its luminosity, effective temperature, and metallicity observed by *Gaia* (Gaia Collaboration 2023). We considered different mixing lengths in the convective envelope and different overshoot and mixing prescriptions above the core (see Appendix C). The weight function, K_r, peaks in two regions in our models: above the convective core, where composition gradients are strong, and below the convective envelope (see Fig. C.1). From one model to another, the relative contribution of these two regions may change significantly. Indeed, when the convective envelope is shallower, the weight of the upper layers increases. As a consequence, $\mathcal{I}$ varies from one model to another, and the measured magnetic field averaged over the radiative region ranges from 140 to 590 G. To go further, since $K_r(r)$ is bimodal, we needed to consider two possibilities: (i) the field is located below the convective envelope or (ii) it is located above the core.

In the first case, an average magnetic field $B_r \approx 140{-}700$ G below the envelope reproduces the observed signature. However, such a field appears to be larger by an order of magnitude than the critical field in this region (see an example in Fig. C.2). Such a magnetic field would be strong enough to suppress g modes (Fuller et al. 2015). Thus, we ruled out this possibility.

For the second scenario, we assumed that a magnetic field is present in the layers above the core that were previously convective. This field is thought to be a remnant of the convective core dynamo-generated field that was left behind when the convective core retreated. In this case, a field $B_r = 4 \pm 0.3$ kG reproduces the observed signature. The error bar reflects the dependence on the star models of KIC 2309579. Moreover, we verified that the value of B_r is below the critical field for all the star models. Therefore, this second scenario is clearly favored.

5. Discussion and conclusion

If the presence of a magnetic field perfectly explains the spectrum of KIC 2309579, we must verify that other phenomena cannot mimic the signature of a magnetic field. We especially considered the presence of glitches, differential rotation, and dips induced by pure inertial modes in the core.

Glitches are expected to occur in γ Dor stars due to the sharp increase of the Brunt-Väisälä frequency above the convective core. However, following Miglio et al. (2008), the frequency shift induced by a glitch for a $\ell = 2$ Kelvin mode is twice the shift for the $\ell = 1$ Kelvin mode with the same radial order. As a consequence, glitches tend to vanish in $\delta K_{\rm a}$ and cannot explain the observed signature.

The effects of radial differential rotation have been studied by Takata et al. (2020). They showed it can be treated within the TAR by considering a rotation that is an average over the mode cavity, which is the same for $\ell = 1$ and 2 Kelvin modes. Moreover, since the latitudinal variation of $\ell = 1$ and $\ell = 2$ Kelvin modes are very similar (see, e.g., Lignières et al. 2024), we expect that latitudinal differential rotation affects $\ell = 1$ and $\ell = 2$ Kelvin modes similarly and cancel out in $\delta K_{\rm a}$.

Finally, in the range of spin parameters reached in this study, $\ell = 1$ Kelvin modes could couple with a purely inertial mode propagating in the convective core, creating a so-called dip (Ouazzani et al. 2020). This induces frequency shifts of modes, creating a feature in $\delta K_{\rm a}$ that could mimic the one produced by a magnetic field. We thus decided to model the spectrum of KIC 2309579 by considering the presence of a dip, following Tokuno & Takata (2022) and Galoy et al. (2024). Results are presented in Appendix B. The model struggles to reproduce both $\ell = 1$ and $\ell = 2$ long-period modes, whereas the magnetic model explains the whole spectra well (see Fig. B.1). Moreover, the coupling factor q between the pure inertial mode and $g{-}i$ modes is large, reaching values that are expected for early MS stars (Galoy et al. 2024), whereas KIC 2309579 is a mid-MS star, according to our models and the models of Fritzewski et al. (2024). In addition, the spin parameter of the inertial mode $s_\star$ has values that are lower than the expected ones (Galoy et al. 2024). To explain this, we could invoke a fast rotating core or the presence of a strong magnetic field inside the core (Barrault et al. 2025a,b). However, in such a case, a decrease of $s_\star$ must be accompanied by a strong decrease of q, which contradicts the observation. We conclude that a dip hardly reproduces the spectrum of KIC 2309579.

We thus detected a near-core magnetic field of $B_r \approx 4$ kG in KIC 2309579. This is the first seismic evidence of a magnetic field in a typical γ Dor star, as the detection by Takata et al. (2026) concerns a star that rotates abnormally slowly for a γ Dor star. Li et al. (2022) proposed that magnetic fields observed in the core of red giants were remnants of core magnetic fields of the MS. The field strength extrapolated by Li et al. (2022) for MS stars is similar to the one found in this paper and in Takata et al. (2026), which is compatible with a convective core dynamo field. The technique we used to analyze this star will be extended to other γ Dor stars observed by spaced-based missions such as *Kepler*, TESS, and, in the very near future, PLATO.

Acknowledgements. We thank the anonymous referee for providing helpful and constructive comments. This work has been supported by CNES, focused on the preparation of the PLATO mission. We thanks M. Deal for his useful advice on stellar modeling, O. Creevey for her precious insight on Gaia measurements, and V. Antoci for useful discussion on spectral analysis. This paper includes data collected by the *Kepler* mission and obtained from the MAST data archive at the Space Telescope Science Institute (STScI). Funding for the *Kepler* mission is provided by the NASA Science Mission Directorate. STScI is operated by the Association of Universities for Research in Astronomy, Inc., under NASA contract NAS 5–26555.

References

Alecian, G., & LeBlanc, F. 2020, MNRAS, 498, 3420
Angulo, C., Arnould, M., Rayet, M., et al. 1999, Nucl. Phys. A, 656, 3
Asplund, M., Grevesse, N., Sauval, A. J., & Scott, P. 2009, ARA&A, 47, 481
Ballot, J., Lignières, F., Prat, V., Reese, D. R., & Rieutord, M. 2012, ASPC Ser., 462, 389
Barrault, L., Mathis, S., & Bugnet, L. 2025a, A&A, 694, A225
Barrault, L., Bugnet, L., Mathis, S., & Mombarg, J. S. G. 2025b, A&A, 701, A253
Benomar, O., Appourchaux, T., & Baudin, F. 2009, A&A, 506, 15
Berthomieu, G., Gonczi, G., Graff, P., Provost, J., & Rocca, A. 1978, A&A, 70, 597
Böhm-Vitense, E. 1958, Z. Astrophys., 46, 108
Borucki, W. J., Koch, D., Basri, G., et al. 2010, Science, 327, 977
Charpinet, S., Green, E. M., Baglin, A., et al. 2010, A&A, 516, L6
Christophe, S., Ballot, J., Ouazzani, R.-M., Antoci, V., & Salmon, S. J. A. J. 2018, A&A, 618, A47
Deheuvels, S., Li, G., Ballot, J., & Lignières, F. 2023, A&A, 670, L16
Dhouib, H., Mathis, S., Bugnet, L., Van Reeth, T., & Aerts, C. 2022, A&A, 661, A133
Fritzewski, D. J., Aerts, C., Mombarg, J. S. G., Gossage, S., & Van Reeth, T. 2024, A&A, 684, A112
Fuller, J., Cantiello, M., Stello, D., Garcia, R. A., & Bildsten, L. 2015, Science, 350, 423
Gaia Collaboration (Vallenari, A., et al.) 2023, A&A, 674, A1
Galoy, M., Lignières, F., & Ballot, J. 2024, A&A, 689, A177
Goodman, J., & Weare, J. 2010, Commun. Appl. Math. Comp. Sci., 5, 65
Hatt, E. J., Ong, J. M. J., Nielsen, M. B., et al. 2024, MNRAS, 534, 1060
Imbriani, G., Costantini, H., Formicola, A., et al. 2004, A&A, 420, 625
Kaye, A. B., Handler, G., Krisciunas, K., Poretti, E., & Zerbi, F. M. 1999, PASP, 111, 840
Lee, U., & Saio, H. 1997, ApJ, 491, 839
Li, G., Van Reeth, T., Bedding, T. R., et al. 2020, MNRAS, 491, 3586
Li, G., Deheuvels, S., Ballot, J., & Lignières, F. 2022, Nature, 610, 43
Li, G., Deheuvels, S., Li, T., Ballot, J., & Lignières, F. 2023, A&A, 680, A26
Lignières, F., Ballot, J., Deheuvels, S., & Galoy, M. 2024, A&A, 683, A2
Manchon, L., Deal, M., Marques, J. P. C., & Lebreton, Y. 2025, A&A, 704, A79
Michaud, G., & Proffitt, C. R. 1993, ASPC Ser., 40, 246
Miglio, A., Montalbán, J., Noels, A., & Eggenberger, P. 2008, MNRAS, 386, 1487
Mombarg, J. S. G., Van Reeth, T., & Aerts, C. 2021, A&A, 650, A58
Morel, P. 1997, A&AS, 124, 597
Morel, P., & Lebreton, Y. 2008, Ap&SS, 316, 61
Mosser, B., Goupil, M. J., Belkacem, K., et al. 2012, A&A, 548, A10
Ouazzani, R.-M., Salmon, S. J. A. J., Antoci, V., et al. 2017, MNRAS, 465, 2294
Ouazzani, R.-M., Marques, J. P., Goupil, M.-J., et al. 2019, A&A, 626, A121
Ouazzani, R.-M., Lignières, F., Dupret, M.-A., et al. 2020, A&A, 640, A49
Prat, V., Mathis, S., Buysschaert, B., et al. 2019, A&A, 627, A64
Prat, V., Mathis, S., Neiner, C., et al. 2020, A&A, 636, A100
Reese, D., Rieutord, M., & Lignières, F. 2006, A&A, 455, 607
Richer, J., Michaud, G., & Turcotte, S. 2000, ApJ, 529, 338
Rogers, F. J., & Nayfonov, A. 2002, ApJ, 576, 1064
Serenelli, A. M. 2010, Ap&SS, 328, 13
Takata, M., Ouazzani, R.-M., Saio, H., et al. 2020, A&A, 635, A106
Takata, M., Murphy, S. J., Kurtz, D. W., Saio, H., & Shibahashi, H. 2026, MNRAS, 545, staf2153
Tokuno, T., & Takata, M. 2022, MNRAS, 514, 4140
Townsend, R. H. D., & Teitler, S. A. 2013, MNRAS, 435, 3406
Verma, K., & Silva Aguirre, V. 2019, MNRAS, 489, 1850
Villate, M., Deheuvels, S., & Ballot, J. 2026, A&A, 707, A366
Zong, W., Charpinet, S., Vauclair, G., Giammichele, N., & Van Grootel, V. 2016, A&A, 585, A22

Appendix A: Magnetic model spectrum

A.1. Asymptotic magnetic model

As described in Sect. 3.1, we modeled the spectrum of KIC 2309579 within an asymptotic approximation of the TAR. Christophe et al. (2018) have shown that the asymptotic TAR is well suited to model g-i mode spectra of rotating stars. Of course, there are some deviations due to non-asymptotic effects, and we must ensure that these deviations do not introduce biases that could lead to false magnetic detections. We then used spectra computed with the 2D oscillation code TOP (Reese et al. 2006) that was used in Lignières et al. (2024), as well as spectra computed with the non-asymptotic TAR oscillation code GYRE (Townsend & Teitler 2013). We computed spectra of a γ Dor star model with a mass of 1.5 $M_\odot$ and a radius 2.2 $R_\odot$ with a rotation of 11.5 μHz. We then fitted our asymptotic model of $\ell = 1$ and $\ell = 2$ Kelvin modes to these synthetic spectra. We found good agreement. We are able to fit simultaneously both series of modes with a common Π_0 and $\nu_{\rm rot}$ by allowing two different values for the phase offset ϵ_g. Values of $\epsilon_{g,1}$ and $\epsilon_{g,2}$ are very close but need to be slightly different to correctly reproduce the spectra. We then added ν_B as a free parameter in the asymptotic model. We fitted our synthetic spectra and verified we recover a value of ν_B compatible with zero.

Similarly to Villate et al. (2026), we decided to introduce a model error, which is quadratically added to the observation errors, to take into account the dispersion of frequencies around the asymptotic model due to non-asymptotic effects. Based on a comparison of asymptotic models to complete computations, we have considered that, for each series of modes, the error of periods is constant in the corotation frame. We thus added two additional free parameters, σ_{ℓ_1} and σ_{ℓ_2}, which are the model error of $\ell = 1$ and $\ell = 2$ Kelvin modes.

Table A.1. Prior distributions for the magnetic model.

Parameter	Distribution	Interval
Π_0 (s)	Uniform	[3000, 5000]
ν_R (μHz)	Uniform	[11, 12]
ϵ_{g_ℓ}	Uniform periodic	[0, 1]
ν_B (μHz)	Modified Jeffrey	$\left[0, 10^{-4}\right]$
σ_{ℓ_1} (s)	Uniform	[0, 2000]
σ_{ℓ_2} (s)	Uniform	[0, 1000]

A.2. Fitting the observations

We fit our model to the observed frequencies by following a Bayesian approach with a Markov chain Monte Carlo (MCMC) method. We defined priors for all parameters of the model. The prior for buoyancy radius Π_0 follows a uniform distribution over [3000, 5000] seconds, which covers the typical Π_0 values for γ Dor stars (Li et al. 2020). Li et al. (2020) also showed that the seismic rotation period remains quite close to the surface one for γ Dor stars. As KIC 2309579 exhibits a rotational modulation at 11.50 μHz (see Appendix D), we set a uniform prior distribution over [11, 12] μHz for $\nu_{\rm rot}$. We set a uniform-periodic prior distribution over [0, 1] for the ϵ_{g_1} and ϵ_{g_2} parameters. Here, "uniform-periodic" means a uniform prior for which the posteriors are the results of steps by the walkers modulo the interval range. As we do not have prior information about the magnetic component ν_B, we used a non-informative distribution, the modified Jeffrey distribution. This prior is a scale-invariant prior over $]10^{-5}, 10^{-4}]$ μHz, and smoothly transitions to a quasi-uniform distribution over $[0, 10^{-5}]$ μHz. Finally, the prior distributions for the model errors σ_{ℓ_1} and σ_{ℓ_2} are uniform over respectively [0, 2000] and [0, 1000] μHz for $\ell = 1$ and $\ell = 2$ modes. The chosen prior distributions of the model parameters are summarized in Table A.1.

We used the asteroseismic Bayesian inference by MCMC (ABIM) code to sample the posterior probabilities. ABIM is a Fortran code parallelized with OpenMP directives, which we have developed. It has been used for example to model mixed mode spectra in red giants in Villate et al. (2026). For the present work, sampling has been performed with a MCMC method implementing the "stretched move" algorithm proposed by Goodman & Weare (2010) and including parallel tempering as described, for example, by Benomar et al. (2009). The latter improved the exploration of parameter spaces containing numerous local maxima. We typically sample the posterior distributions with 20 parallel chains and 300 walkers for each chain. The initial positions of the walkers are randomly drawn from the prior distributions. The walkers are iterated over 15 000 steps, with the 5 000 first steps discarded as burn-in to ensure that chains are stationary. After the sampling process, we assessed the completeness of the sampling for every parameter by looking at the shape of the posterior distributions and by checking the correlation times. They are defined as the number of steps needed for the autocorrelation function of the chain to be divided by e. In our case, the correlation time is about 37, which ensures to get about 81 000 uncorrelated sampling points.

As a result of the sampling, the median of the posterior distributions of the model parameters and the 1σ errors are presented in Table A.2. The values of ϵ_{g_1} and ϵ_{g_2} remain quite close and the estimated $\nu_{\rm rot}$ is coherent with the one found with the rotational modulation. We find a significant detection for the magnetic field since $\nu_B = 46.8 \pm 3.4$ pHz. To verify the sensitivity of our analysis to the selected frequencies, we also performed analyses by rejecting frequencies below a 5σ detection level (instead of 4σ), that is a S/N of 5.1, and frequencies which are combinations within 3σ error bars (instead of 2σ), that is removing also f_{66}, f_{28}, f_{44}, f_{45}, f_{68} and f_{71}. The determination of ν_B only slightly changes (decreased by less than 10%), is still highly significant, and does not change the conclusion of this paper.

Appendix B: Model spectrum with a dip

We adapted the model proposed by Tokuno & Takata (2022) and Galoy et al. (2024) to couple g-i modes with a pure inertial mode. We computed the spectrum of mixed inertial/g-i modes by finding the roots of

$$\cot\theta_{\rm g} = \frac{q}{s_\star - s}, \tag{B.1}$$

where

$$\theta_{\rm g} = \pi\left(\frac{s - s_{\rm g}}{\Delta s_{\rm g}} - \frac{1}{2}\right), \tag{B.2}$$

$$s_{\rm g} = \frac{2\nu_{\rm rot}\Pi_0}{\sqrt{\Lambda_{\ell,m}}}\left(n + \epsilon_{g_\ell}\right). \tag{B.3}$$

The factor q is the strength of the coupling between the modes

Table A.2. Estimated seismic parameters for the magnetic model.

Π_0 (s)	ν_R (μHz)	ϵ_{g_1}	ϵ_{g_2}	ν_B (pHz)	σ_{ℓ_1} (s)	σ_{ℓ_2} (s)
3884 ± 31	11.501 ± 0.015	0.562 ± 0.282	0.563 ± 0.275	46.8 ± 3.4	76^{+28}_{-19}	46^{+13}_{-9}

(denoted σ in Galoy et al. 2024), $s_\star$ the spin parameter of the inertial mode, and s_g the spin parameters of the g-i modes. The separation Δs_g denotes the difference of spin parameters of modes with consecutive n. This model relies on six free parameters: Π_0, $\nu_{\rm rot}$, $\epsilon_{\rm g_1}$, $\epsilon_{\rm g_2}$, $s_\star$ and q.

We fitted this model to the observations with the method described in Sect. A.2. We used the same prior distributions for the buoyancy radius, the rotation frequency, the gravity offsets and the model error parameters as those used for the magnetic model. The prior of $s_\star$ follows a uniform law over [7, 9.5] to cover the possible spin parameter range within which the coupling could occur, according to the oscillation spectrum of KIC 2309579. Following Galoy et al. (2024), we set a uniform prior over [0.1, 2] for q. The prior distributions of the parameters are summarized in Table B.1. Table B.2 presents the median and the 1σ error bars of the parameters deduced from posterior distributions. Figure B.1 displays the échelle diagrams of both $\ell = 1$ and $\ell = 2$ Kelvin modes observed and modeled frequencies. This model struggles to reproduce all the observed frequencies, contrary to the magnetic model.

Table B.1. Prior distributions for the dip model.

Parameter	Distribution	Interval
Π_0 (s)	Uniform	[3000, 5000]
ν_R (μHz)	Uniform	[11, 12]
ϵ_{g_ℓ}	Uniform periodic	[0, 1]
$s_\star$	Uniform	[7, 9.5]
q	Uniform	[0.1, 2]
σ_{ℓ_1} (s)	Uniform	[0, 2000]
σ_{ℓ_2} (s)	Uniform	[0, 1000]

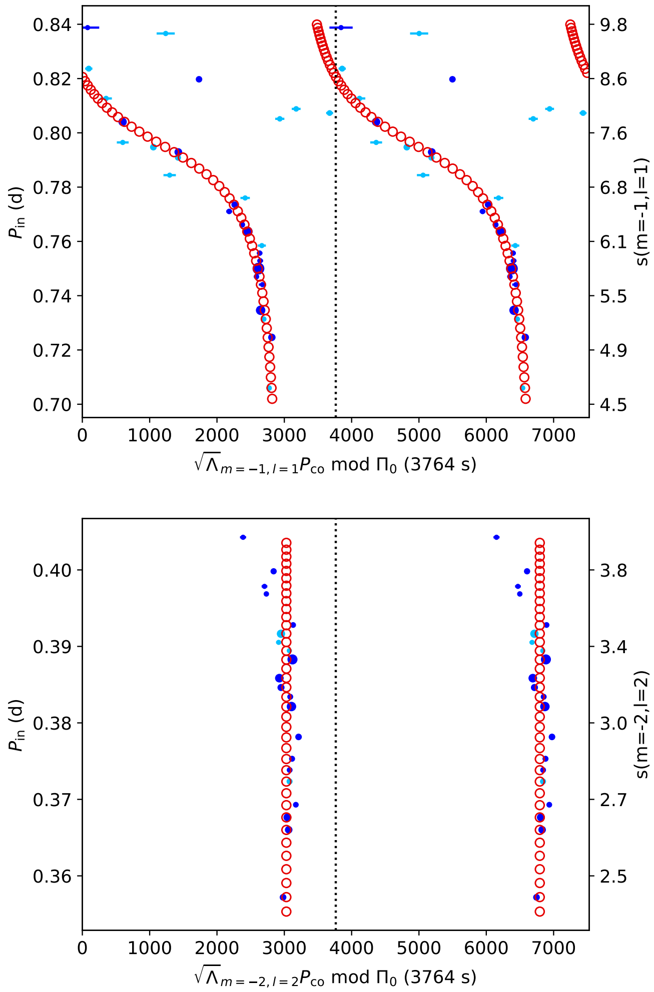

Fig. B.1. Stretched period échelle diagram of $\ell = 1$ (top) and $\ell = 2$ (bottom) mode frequencies. Navy blue dots: observed frequencies used for the analysis. Light blue dots: observed frequencies that are possible frequency combinations and not used for the analysis. Red circles: best-model frequencies. The size of the dots is proportional to the mode amplitude.

Appendix C: Structure model of KIC 2309579

We computed for our study structure models calibrated on KIC 2309579. We calibrated the model with its buoyancy radius ($\Pi_0 = 3880 \pm 100$ s). We used measurements reported in the *Gaia* DR3 (Gaia Collaboration 2023) for its effective temperature ($T_{\rm eff} = 6938 \pm 38$ K), it surface metallicity ($(Z/X)_s = 0.0108 \pm 0.0035$) and its bolometric luminosity. For the latter, we find two significantly different values in the *Gaia* DR3: the GSP-Phot luminosity $L/L_\odot = 10.49 \pm 0.90$ and the FLAME luminosity $L/L_\odot = 8.68 \pm 0.25$. We thus made models calibrated with this two values.

Models have been computed using the `CESAM2k20` code (Morel 1997; Morel & Lebreton 2008; Manchon et al. 2025) and the Optimal Stellar Models (OSM) package. Mass and age are free parameters (mainly constrained by $T_{\rm eff}$ and L). We adopted a solar metal mixture (Asplund et al. 2009) with meteoritic abundances for refractory elements from Serenelli (2010). The initial metallicity $(Z/X)_i$ is a free parameter (mainly constrained by $(Z/X)_s$), and we considered three values for the initial helium abundance $Y_i = 0.25$, 0.26 and 0.27. We used opacity tables from OPAL, the OPAL2005 equation of state (Rogers & Nayfonov 2002) and the nuclear reaction rates from the NACRE collaboration (Angulo et al. 1999) except for the ^{14}N(p, γ)^{15}O reaction, for which we used the LUNA reaction rate given in Imbriani et al. (2004). Convection was treated using the mixing-length theory (Böhm-Vitense 1958) with a mixing-length parameter $\alpha_{\rm MLT} = 1.77$, close to a solar calibration, $\alpha_{\rm MLT} = 1.0$, or $\alpha_{\rm MLT} = 0.5$. Models include the effect of atomic diffusion following the Michaud & Proffitt (1993) formalism with radiative acceleration of Alecian & LeBlanc (2020). We adopted the Montreal prescription (Richer et al. 2000) for turbulent diffusion, calibrated with the parameterization of Verma & Silva Aguirre (2019). Models include also overshooting of the convective

Table B.2. Estimated seismic parameters for the dip model.

Π_0 (s)	ν_R (μHz)	ϵ_{g_1}	ϵ_{g_2}	$s_\star$	q	σ_{ℓ_1} (s)	σ_{ℓ_2} (s)
3912^{+66}_{-127}	$11.552^{+0.029}_{-0.067}$	0.082 ± 0.324	0.92 ± 0.33	$7.74^{+0.38}_{-0.44}$	$1.13^{+0.59}_{-0.38}$	$2.78^{+3.25}_{-2.57}$	$4.60^{+1.50}_{-9.55}$

core with three prescriptions: (i) diffusive overshoot, (ii) instant mixing overshoot, (iii) instant mixing overshoot with adiabatic extension of the core. The overshoot parameter is free, mainly calibrated to reproduce Π_0. The overshoot needed to reproduce Π_0 is typically $0.23 \sim 0.29 H_p$ for instant mixing or $0.024 \sim 0.028$ for diffusive mixing. These values are consistent with the study of Mombarg et al. (2021). We also computed a fourth series of models with a fixed overshoot of $0.1 H_p$, but with a free extra uniform turbulent diffusion in the radiative zone, to build models similar to the γ Dor models of Ouazzani et al. (2020). We need a diffusion coefficient $D_t = 600 \sim 750$ cm^2 s^{-1} to fit the observations. Here we used different overshoot or turbulent mixing prescriptions to mimic any mixing processes that would impact these layers (for example, rotational mixing).

We ended up with 72 models with masses from 1.36 to $1.56 M_\odot$ with central hydrogen ranging between 0.25 and 0.38, that is between one half and two third of the central hydrogen reservoir has been burned. We used these different models to explore the influence of modeling uncertainties on the magnetic field strength determination. The value of Y_i has almost no impact, $\alpha_{\rm MLT}$ has a strong impact on the upper layers, the amplitude of $K_r(r)$ below the convective zone and the value of $\mathcal{I}$, but finally no impact on the measured value of magnetic field above the core. The overshoot and mixing prescription changes the shape of the Brunt-Väisälä frequency above the convective core and thus the detailed shape of $K_r(r)$, but it only weakly affects the estimated magnetic field strength in this region.

Figure C.2 displays the critical magnetic field profile B_c in a model of KIC 2309579 computed for the lowest $\ell = 1$ mode frequency (f_{66}). We verify that, near the core, the magnetic field measured in KIC 2309579 (about 4 kG) is lower than B_c. As B_c increases with the frequency, the measured field remains lower than B_c for all the observed modes. We performed this computation with our 72 models and verified that a field $B_r \approx 4$ kG remains below B_c for all of them.

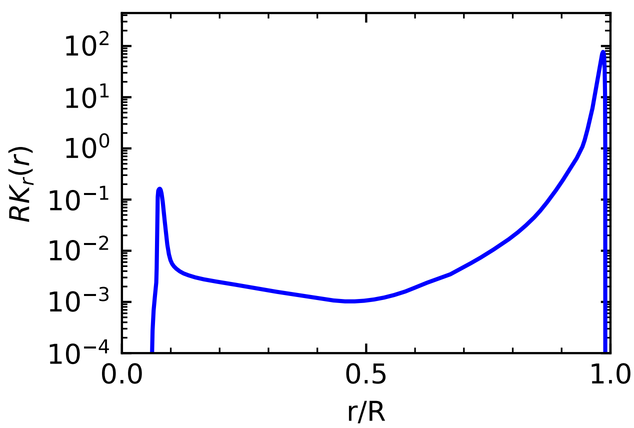

Fig. C.1. Magnetic weight function $K_r(r)$ adimensionalized by the stellar radius R as a function of the normalized radius r, computed for a model of KIC 2309579.

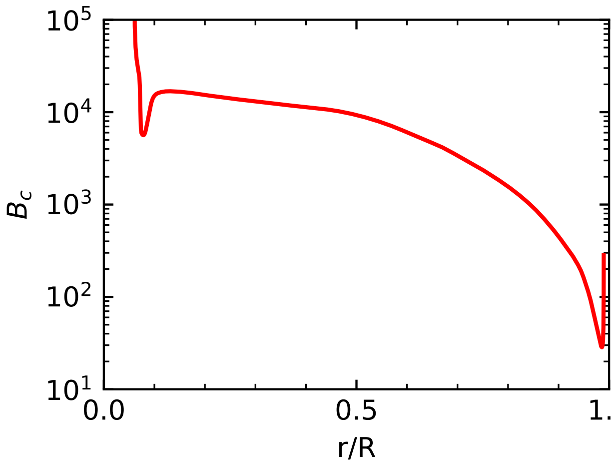

Fig. C.2. Critical magnetic field as a function of the radius, plotted for a representative model of KIC 2309579 with $Y_i = 0.26$, a diffusive overshoot and calibrated of the GSP-Phot luminosity (see text).

Appendix D: Extracted frequencies of KIC 2309579

We performed the analysis of the light curve of KIC 2309579 with a prewhitening technique using the `FELIX` code (Charpinet et al. 2010; Zong et al. 2016). We extracted frequencies with a signal-to-noise ratio greater than 4.7, that is a 4σ detection level. Figure D.1 displays the oscillation spectrum of KIC 2309579. Table D.1 lists the extracted frequencies along with their errors, amplitudes, and signal-to-noise ratios. Since linear combinations and/or harmonics could arise, we specify the possible linear combinations within 2σ error bars. We clearly identified $\ell = 1$ and $\ell = 2$ Kelvin modes as groups of peaks around 15 and 30 μHz. We also identify a peak around 11.50 μHz as the surface rotation $\nu_{\rm rot}$, as well as its harmonics at 2, 3, $4\nu_{\rm rot}$. During the prewhitening process, the rotation peak has been fitted with two very close large peaks, f_{01} and f_{02}, with different phases, presumably to take into account a modulation of its amplitude, which could be due to the finite lifetime of surface spots, latitudinal differential rotation, or even time variations of surface chemical inhomogeneities. Near the rotation frequency, there are a few frequencies that could be identified as Rossby modes and would require a dedicated analysis.

For the frequencies that have been modeled during the analysis, Table D.1 shows their associated degree ℓ and azimuthal order m. We also carried out an a posteriori identification of their radial orders n considering the optimal parameters of our model. Frequencies that could be linear combinations within a 2σ error bar but are well represented by our best-model are noted with a question mark next to their radial orders.

Table D.1. Extracted frequencies of KIC 2309579.

	f (μHz)	σ_f (nHz)	Amplitude (ppm)	S/N	ℓ	m	n	Comments
f_{24}	3.02154171	0.4020	29.2	10.87				
f_{59}	4.69837667	0.8870	10.2	4.93				$f_{66} - f_{04} : 0.6\sigma$
f_{46}	8.61462975	0.5335	13.8	8.19				$f_{13} - f_{49} : 1.2\sigma$
f_{35}	9.55865285	0.3598	21.1	12.15				
f_{20}	9.96821817	0.2120	35.4	20.62				
f_{27}	10.4014541	0.2974	25.1	14.70				
f_{58}	10.9760210	0.7264	10.4	6.02				
f_{37}	11.0792432	0.4050	18.8	10.79				$f_{74} - f_{29} : 0.3\sigma$
f_{15}	11.0894796	0.1504	50.4	29.06				$f_{41} - f_{29} : 1.7\sigma$
f_{25}	11.1814386	0.2739	27.6	15.96				
f_{63}	11.4760733	0.8350	9.2	5.24				
f_{02}	11.4985523	0.0079	973.4	552.88				
f_{01}	11.4988648	0.0076	1016.5	577.38				$\nu_{\rm rot}$
f_{66}	13.7988610	0.928	8.6	4.71	1	−1	117	
f_{57}	13.8345810	0.7460	10.7	5.86	1	−1	115?	$f_{04} - f_{14} : 0.7\sigma$
f_{33}	14.0521910	0.3550	21.9	12.32				$f_{04} - f_{06} : 0.3\sigma$
f_{22}	14.1193500	0.2380	32.8	18.40	1	−1	102	
f_{53}	14.2420280	0.6490	11.9	6.74				$f_{08} - f_{06} : 1.1\sigma$
f_{43}	14.3097500	0.5200	14.8	8.41	1	−1	95?	$f_{39} - f_{05} : 1.0\sigma$
f_{38}	14.3367620	0.4170	18.5	10.48	1	−1	94?	$f_{16} - f_{06} : 0.1\sigma$
f_{47}	14.3748500	0.5620	13.8	7.78				$f_{04} - f_{03} : 0.2\sigma$
f_{09}	14.3949860	0.1000	77.6	43.93	1	−1	92	
f_{60}	14.5318290	0.806	9.6	5.42				$f_{07} - f_{06} : 0.8\sigma$
f_{19}	14.5636310	0.2180	35.6	20.08	1	−1	87?	$f_{08} - f_{03} : 1.5\sigma$
f_{12}	14.5969310	0.1260	61.5	34.63	1	−1	86	
f_{28}	14.6347660	0.3270	23.7	13.38	1	−1	85	
f_{72}	14.7551170	0.9710	8.0	4.50				$f_{56} - f_{10} : 0.0\sigma$
f_{62}	14.9149600	0.8060	9.6	5.43	1	−1	78?	$f_{07} - f_{54} : 0.5\sigma$
f_{23}	14.9627470	0.2370	32.6	18.43	1	−1	77	
f_{44}	15.0109300	0.5300	14.6	8.24	1	−1	76	
f_{32}	15.1066030	0.3470	22.2	12.61	1	−1	74	
f_{05}	15.1565570	0.0650	118.3	67.35	1	−1	73	
f_{64}	15.2600990	0.8320	9.1	5.25	1	−1	71?	$f_{30} - f_{52} : 1.1\sigma$
f_{50}	15.3161150	0.5820	12.9	7.51	1	−1	70	
f_{54}	15.3731870	0.6380	11.7	6.86	1	−1	69	
f_{03}	15.4324980	0.0370	199.5	116.93	1	−1	68	
f_{45}	15.4936900	0.5200	143	8.41	1	−1	67	
f_{68}	15.5547920	0.8760	8.5	4.99	1	−1	66	
f_{06}	15.7551690	0.0660	111.2	66.02	1	−1	63	
f_{52}	15.8252880	0.6090	12.1	7.18	1	−1	62	
f_{14}	15.9721310	0.1380	53	31.70	1	−1	60	
f_{42}	16.3945560	0.4770	14.8	9.17	1	−1	55	
f_{17}	22.9982834	0.1672	3.9	26.14				$2\nu_{\rm rot}$
f_{49}	23.0056685	0.5069	13.0	8.63				
f_{65}	28.6298020	0.7240	9.0	6.04	2	−2	94	
f_{26}	28.9481710	0.2420	26.8	18.05	2	−2	89	
f_{71}	29.0917110	0.7920	8.2	5.52	2	−2	87	
f_{51}	29.1641860	0.5220	12.5	8.37	2	−2	86	
f_{39}	29.4656660	0.3490	18.4	12.53	2	−2	82	
f_{10}	29.5517980	0.0830	77.0	52.47	2	−2	81?	$f_{05} + f_{09} : 1.8\sigma$
f_{75}	29.6369050	0.8350	7.7	5.24	2	−2	80?	$f_{32} + f_{60} : 1.3\sigma$
f_{67}	29.7197070	0.7570	8.5	5.77	2	−2	79?	$f_{05} + f_{19} : 0.6\sigma$
f_{04}	29.8072560	0.0490	130.8	88.72	2	−2	78	
f_{08}	29.9964790	0.0740	8.5	59.10	2	−2	76	
f_{16}	30.0918700	0.1400	45.1	31.15	2	−2	75	
f_{34}	30.1868560	0.2950	21.2	14.82	2	−2	74	
f_{07}	30.2876270	0.0570	110.3	76.20	2	−2	73	
f_{21}	30.6058160	0.1840	34.2	23.81	2	−2	70	
f_{31}	30.8387980	0.2740	22.7	15.96	2	−2	68	

Table D.1. Continued.

	f (μHz)	σ_f (nHz)	Amplitude (ppm)	S/N	ℓ	m	n	Comments
f_{36}	30.9602270	0.3200	19.4	13.68	2	−2	67	
f_{30}	31.0842580	0.2700	23.1	16.21	2	−2	66	
f_{49}	31.3406810	0.3480	18	12.57	2	−2	64	
f_{11}	31.4812770	0.0960	66	45.75	2	−2	63	
f_{13}	31.6211660	0.1120	56.6	39.18	2	−2	62	
f_{18}	32.4025250	0.1710	36.5	25.54	2	−2	57	
f_{48}	34.4967813	0.4725	13.1	9.25				$3\nu_{\rm rot}$
f_{61}	34.5062545	0.6454	9.6	6.77				
f_{77}	42.7489582	0.7814	6.9	5.59				
f_{56}	44.3069656	0.5265	10.7	8.30				$f_{22} + f_{34} : 1.2\sigma$
f_{29}	44.3578455	0.2397	23.6	18.23				$f_{41} - f_{15} : 1.7\sigma$
f_{69}	44.6887790	0.6609	8.5	6.61				$f_{12} + f_{16} : 0.0\sigma$
f_{79}	45.5615112	0.8607	6.6	5.08				$f_{06} + f_{04} : 1.1\sigma$
f_{76}	45.7122074	0.7496	7.6	5.83				$f_{32} + f_{21} : 0.3\sigma$
f_{70}	45.9956586	0.7058	8.2	6.19				$4\nu_{\rm rot}$
f_{74}	55.4373428	0.7120	7.8	6.14				
f_{41}	55.4465469	0.3666	15.2	11.93				$f_{15} + f_{29} : 1.7\sigma$
f_{78}	58.4258909	0.8226	6.7	5.31				
f_{73}	59.5550624	0.7023	7.9	6.23				$f_{26} + f_{21} : 1.4\sigma$
f_{55}	59.7386007	0.4777	11.6	9.15				$f_{10} + f_{34} : 0.1\sigma$

Notes. In the first column, the frequencies are labeled according to their amplitudes. In the *Comments* column, possible linear combinations within 2σ are listed in the form $f_a \pm f_b : n\sigma$ and rotation frequency and its first harmonics are noted in the form $n\ \nu_{\rm rot}$.

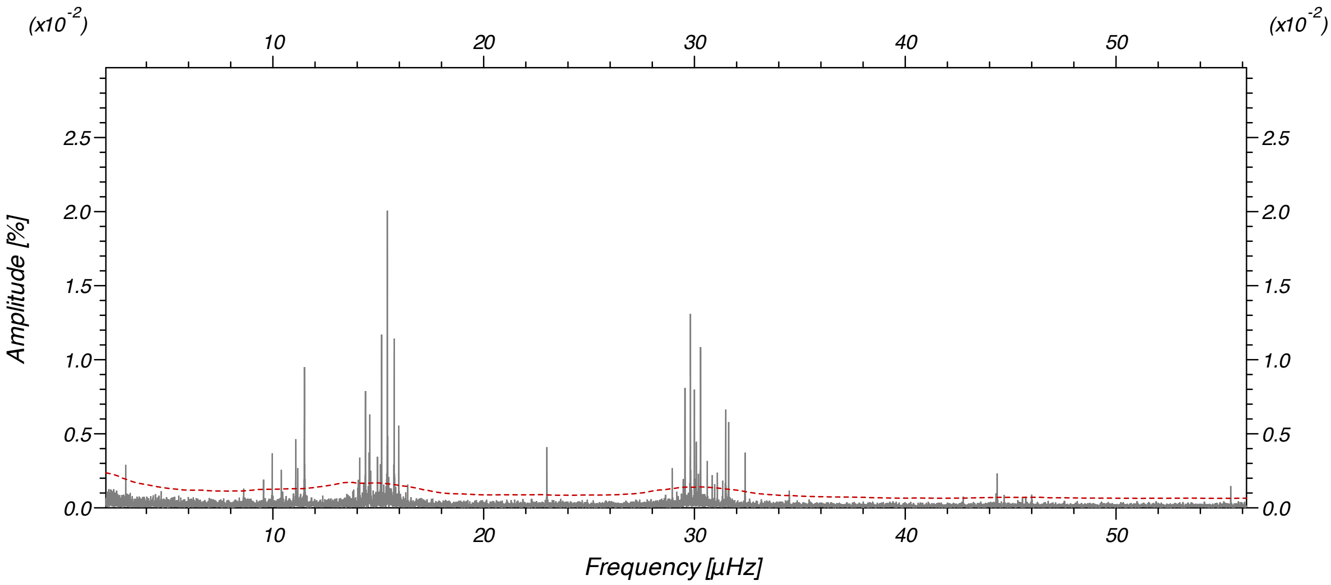

Fig. D.1. Oscillation spectrum of KIC 2309579. The frequency axis is represented in μHz, and the amplitude axis is represented in %. The dashed red curve represents the 4σ noise threshold before prewhitening.